Supplementary Information for

Orbital Engineering Activated Intrinsic Conduction Enables Ultra-high-rate Performance Zinc Storage in Manganese Dioxide

Huihui Hu[1]†, Yanhong Feng[1]†, Zhiwei Wang[1], Longchao Zhuo[2], Cejun Hu[3]*, Imran Shakir[4], Dingsheng Wang[5], and Xijun Liu[1]**

[1] *MOE Key Laboratory of New Processing Technology for Nonferrous Metals and Materials, Guangxi Key Laboratory of Processing for Non-ferrous Metals and Featured Materials, School of Resources, Environment and Materials, Guangxi University, Nanning, 530004 Guangxi, China*

[2] *School of Materials Science and Engineering, Xi'an University of Technology, Xi'an, 10048, China*

[3] *College of Materials Science and Engineering, Fuzhou University, Fuzhou, 350108 Fujian, China*

[4] *Department of Physics, Faculty of Science, Islamic University of Madinah, Madinah 42351, Saudi Arabia*

[5] *Department of Chemistry, Tsinghua University, 100084, Beijing, China*

*****Corresponding authors: fyh0811@gxu.edu.cn; cejun_hu@fzu.edu.cn; xjliu@gxu.edu.cn;

† These authors contributed equally: Huihui Hu, Yanhong Feng

Experimental section

Synthesis of Fe_x-MnO_2, and MnO_2 cathodes (x= 0.01, 0.02, 0.015)

Take the $Fe_{0.015}$-MnO_2 (abbreviated as Fe-MnO_2) sample for example, first, 0.3 mM of $KMnO_4$ and 0.015 mM $Fe(NO_3)_3 \cdot 9H_2O$ were added into 40 mL of deionized water (DI) under magnetic stirring. Then, 0.06 mM of $MnSO_4 \cdot H_2O$ was added into the above solution and stirred for another 20 min. A piece of carbon cloth (4 cm × 3 cm) was put into the above solution, transferred into a Teflon-lined stainless steel autoclave and heated at 120℃ for 1.5 h. After cooling down to room temperature, the obtained Fe-MnO_2 was washed with DI water three times, and dried in a vacuum oven at 60℃ for 8 h. The method for synthesizing $Fe_{0.01}$-MnO_2 and $Fe_{0.02}$-MnO_2 samples as above with the content of $Fe(NO_3)_3 \cdot 9H_2O$ were 0.01 mM and 0.02 mM, respectively. And the method for synthesizing MnO_2 sample also as above but not added $Fe(NO_3)_3 \cdot 9H_2O$. All the materials were directly used as cathodes without any binders and conducting agents.

Materials characterization

Bruker D8 X-ray diffractometer (Bruker XRD Goniomerter, A24A10) was used for testing the crystal information. The Operando XRD (model ARLEquinox3000) from ThermoFisher USA, was used with an operating voltage of 40 kV, a current of 40 mA, a scanning range of 10-80°, and a test time of 10 min. Scanning electron microscope (SEM) images were obtained on a Zeiss in-situ SEM (sigma 300) for testing the morphology. Transmission electron microscopy (TEM) images and energy dispersive X-ray spectroscopy (EDX) mapping were obtained by an FEI Talos F200X S/TEM with an FEG for testing the structure and elements. X-ray absorption spectroscopy including X-ray absorption near edge structure (XANES) and extended X-ray absorption fine structure (EXAFS) measurements were performed by using the tabletop X-ray absorption fine structure spectrometer (Anhui Specreation Instrument Technology Co., LTD, TableXAFS-500A). The spectra were recorded in the fluorescence mode of the monochromator equipped with a passivated implanted planar silicon detector. X-ray photoelectron spectroscopy (XPS) measurements using Thermo

ESCALAB 250 XI + Spectrometer for testing valence state. Brunauer-Emmett-Teller (BET) surface area measurements were performed through nitrogen sorption on Micromeritics ASAP 2460. Inductively coupled plasma optical emission spectrometry (ICP-OES) data were collected on Agilent 7700 to determine the content of elements in solution. Conductivity is tested as a function of pressure by means of a four-probe, type ST2722B. Cyclic voltammetry (CV) tests and electrochemical quartz crystal microbalance (EQCM) measurements were performed on a CHI440C (CH Instruments) electrochemical workstation. Ultraviolet-visible spectroscopy (Fig. S24) absorption spectrum was obtained using a UV-1800PC spectrophotometer (Shanghai Jinghua Technology Instrument Co., Ltd.).

Electrochemical measurements

For punch-cell, the Fe-MnO_2 were directly used as cathodes without cut with the mass loading of active material was ~1.33 mg cm^{-2} for packaging, electrode area was 3×4 cm^2, electrolyte volume was ~1 mL. For coin-cell, the MnO_2 and Fe-MnO_2 were diced into 12 mm diameter circles and used as the working electrodes with the mass loading of active material was around 0.8-1.2 mg, electrode area and electrolyte volume were 1.13 cm^{-2} and 100 μL, respectively. The reference electrode using Zn foil with 0.15 mm thickness and the aqueous solution containing $ZnSO_4$ (2 M) and $MnSO_4$ (0.1 M) used as electrolyte. Glass fiber membrane (GF/D) used as the separator. The galvanostatic charge/discharge (GCD) was tested in a NEWARE battery test system (BTS80) under the voltage range of 0.8-1.85 V. Cyclic voltammetry (CV) measurements were tested in an electrochemical workstation (CHI 660E). *In-situ* electrochemical impedance spectroscopy (*In-situ* EIS) was measured on an DH7003B electrochemistry workstation by sweeping the frequency from 100 kHz to 0.01 Hz with an alternating current amplitude of 5 mV. For galvanostatic intermittent titration technique (GITT) measurement, the cell was discharged/charged for 5 min at 200 mA g^{-1}, followed by a 60 min relaxation process to reach the voltage equilibrium. The ion diffusion coefficient was calculated by the following equation:

$$D_{GITT} = \frac{4}{\pi\tau}\left(\frac{n_m V_m}{S}\right)^2\left(\frac{\Delta Es}{\Delta E\tau}\right)^2$$

where τ, n_m, V_m, and S presented the constant current pulse duration, the amount of active material, molar volume, and the electrode-electrolyte interface, respectively. ΔE_s was the steady-state voltage change under the current pulse. ΔE_τ was voltage change under the constant current pulse after the eliminating of *iR* drop.

The Mn^{2+} concentration using formaldehyde oxime spectrophotometry under UV-vis, respectively. The standard curve was established using standard solutions containing 2 M $ZnSO_4$ and varying concentrations (0, 0.02, 0.04, 0.08, 0.15 M) of $MnSO_4$. The linear regression equation obtained was: y = 6.176 x + 0.137, with a correlation coefficient: r = 0.99963.

EQCM measurements were performed using a two-electrode system with a gold quartz crystal resonator as the working electrode and zinc foil as the counter and reference electrodes. For sample preparation of the EQCM, Au-coated quartz crystals were coated using a pipette with a slurry containing 80 wt.% Fe-MnO_2 powder, 10 wt.% of Super P, and 10 wt.% of polyvinylidene fluoride binder in N-methyl-2-pyrrolidone. The electrolyte was 2 M $ZnSO_4$ together with 0.1 M $MnSO_4$. EQCM experiments rely on the calculation of mass change (Δm) at the quartz crystal using the measured frequency change (Δf) as given by the Sauerbrey equation:

$\Delta f = -2f_0^2/[A\ (\mu\rho)^{1/2}]\ \Delta m$,

where f_0 is the resonant frequency of the fundamental mode of the crystal, A is the area of the gold disk coated onto the crystal (0.205 cm^2 for the included crystal), ρ is the density of the crystal, and μ is the shear modulus of quartz. The density of the crystal is 2.648 g cm^{-3} and the shear modulus μ is 2.947×10^{11} g/cm s^2. For an 8 MHz crystal, a 0.1 Hz change in frequency corresponds a mass change of 0.14 ng.

Density functional theory (DFT) calculation methods

DFT calculations were performed using the Vienna Ab-initio Simulation Package (VASP) with a supercell of $2\times2\times1$[1, 2]. The gradient-corrected exchange correlation functional of Perdew-Burke-Ernzerh generalized-gradient-approximation (PBE-GGA)

was employed. In order to more accurately describe the d orbitals of transition metals, the DFT+U method was used. The effective U values given to Fe and Mn ions were 5.3 eV, and 3.9 eV, respectively. The computational process also encompassed magnetic calculations, with Mn and Fe values set at 3 and 5. A plane-wave basis with 520 eV energy cut-off was adopted using the projector augmented wave (PAW) basis-set and the converge criteria of the force on each relaxed atom below 0.01 eV $Å^{-1}$ were used. The convergence criteria were chosen such that the changes were 10^{-5} eV for the energy. The equilibrium lattice constants of MnO_2 unit cell were optimized when using a 5 × 5 × 1 monkhorst pack K-point grid for Brillouin zone sampling. The Brillouin zone integral utilized the surfaces structures of 3 × 3 × 1 monkhorst pack K-point sampling. While the MnO_2 crystal consists of 32 Mn and 64 O atoms, the Fe-MnO_2 is composed of 30 Mn, 2 Fe, and 64 O atoms. Every atom in these two models underwent relaxation. The adsorption energies (*E*ads) were calculated as *E*ads = *E*ad/sub - *E*ad - *E*sub, where *E*ad/sub, *E*ad, and *E*sub are the optimized adsorbate/substrate system, the adsorbate, and the clean substrate, respectively. The climbing imagenudged elastic band (CI-NEB) method was employed to calculate the Zn ion migration barrier[3]. The calculation of the diffusion barrier of Zn was performed on two models of Fe-MnO_2 and MnO_2.

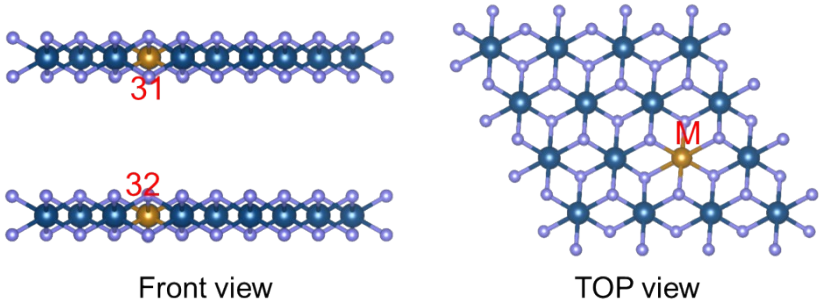

Fig. S1 The Front view and TOP view of the stable M-MnO_2 configurations (M: Fe, Mg, Ca, Ni, Ag, Cu, Co).

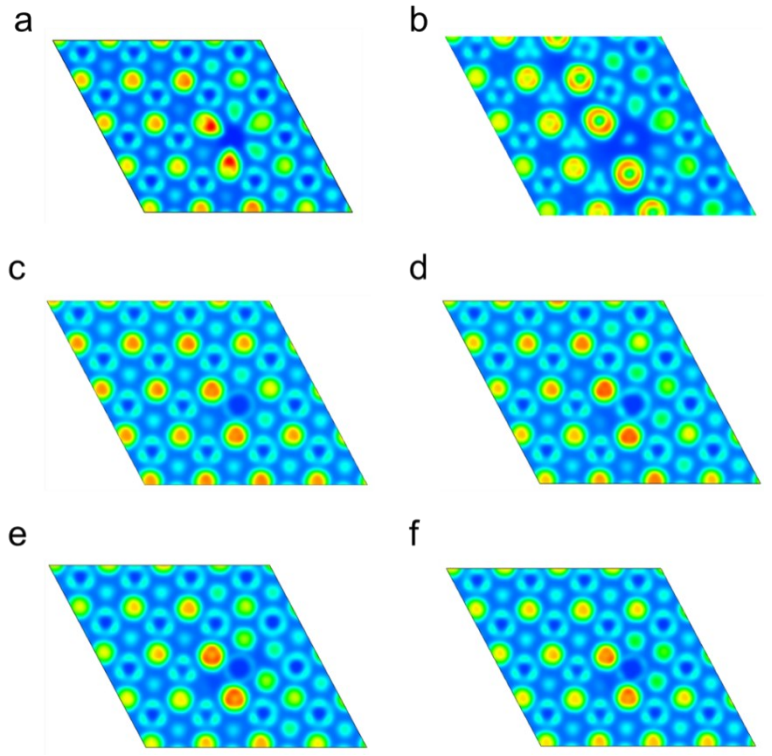

Fig. S2 The electron localization function of (a) Mg-MnO_2, (b) Ca-MnO_2, (c) Ni-MnO_2, (d) Ag-MnO_2, (e) Cu-MnO_2, and (f) Co-MnO_2 configuration.

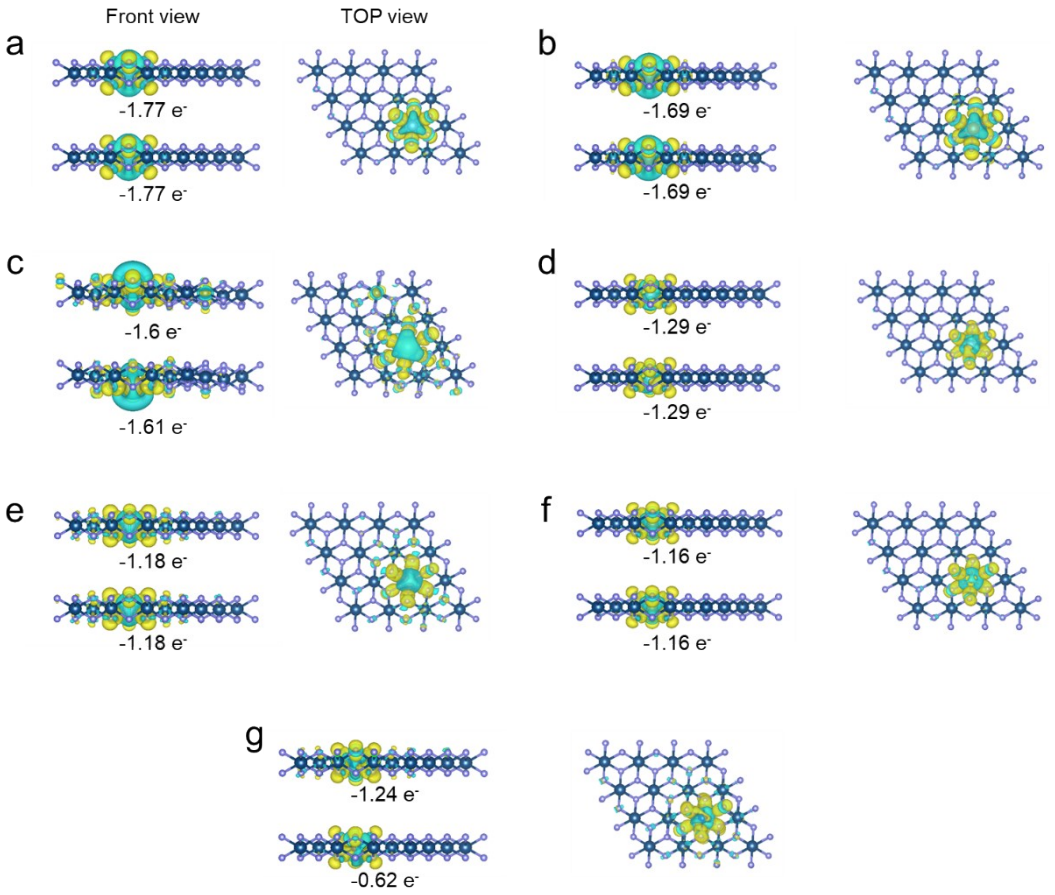

Fig. S3 Difference charge density map of the stable (a) Fe-MnO_2, (b) Mg-MnO_2, (c) Ca-MnO_2, (d) Ni-MnO_2, (e) Ag-MnO_2, (f) Cu-MnO_2, and (g) Co-MnO_2 configuration, where blue color indicates electron loss and yellow color indicates electron accumulation. The numbers on the difference charge density are the corresponding Bader charge values.

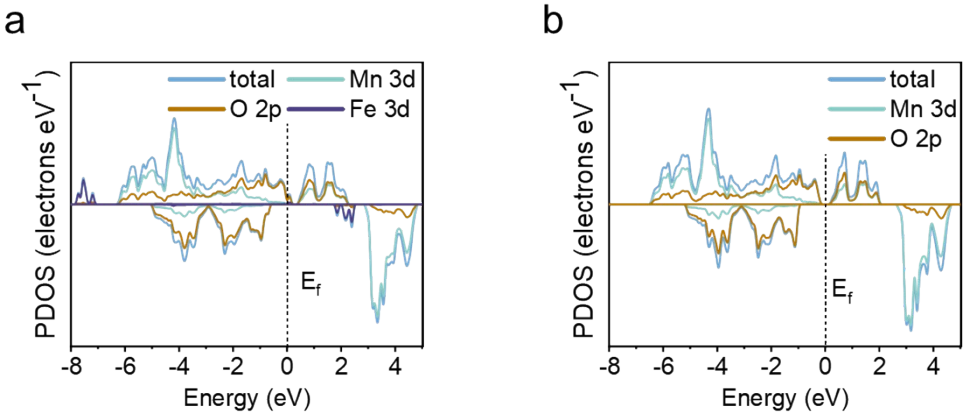

Fig. S4 Calculated PDOS of (a) Fe-MnO_2 and (b) MnO_2 with aligned Fermi level.

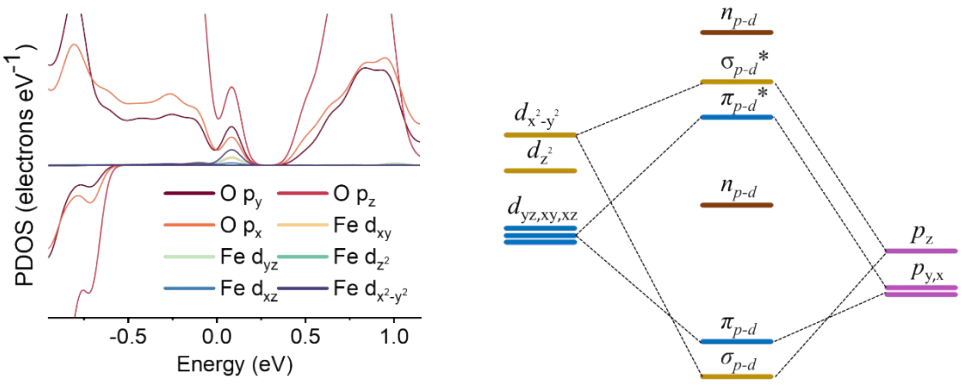

Fig. S5 The detailed PDOS for the Fe 3d and O 2p orbitals of Fe-MnO_2 and orbitals hybridization.

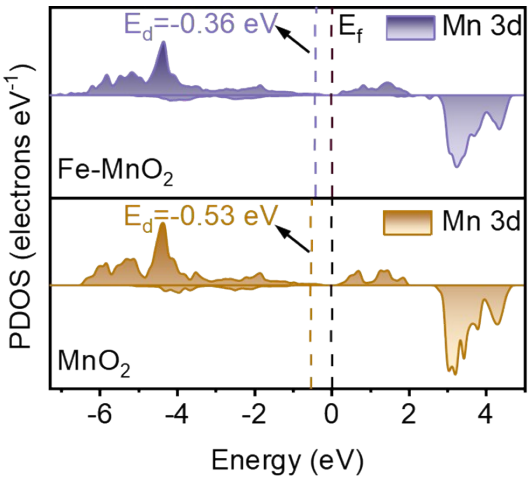

Fig. S6 The PDOS of Fe-MnO_2 and MnO_2 relative to the d-band center of the Fermi energy level.

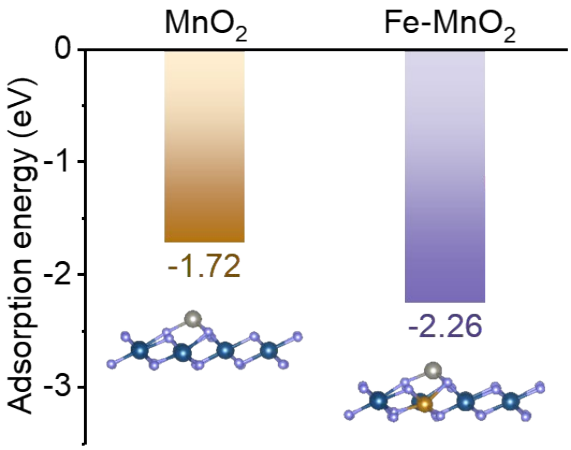

Fig. S7 Zn^{2+} adsorption energy in MnO_2 and Fe-MnO_2 configurations and their schematic diagrams.

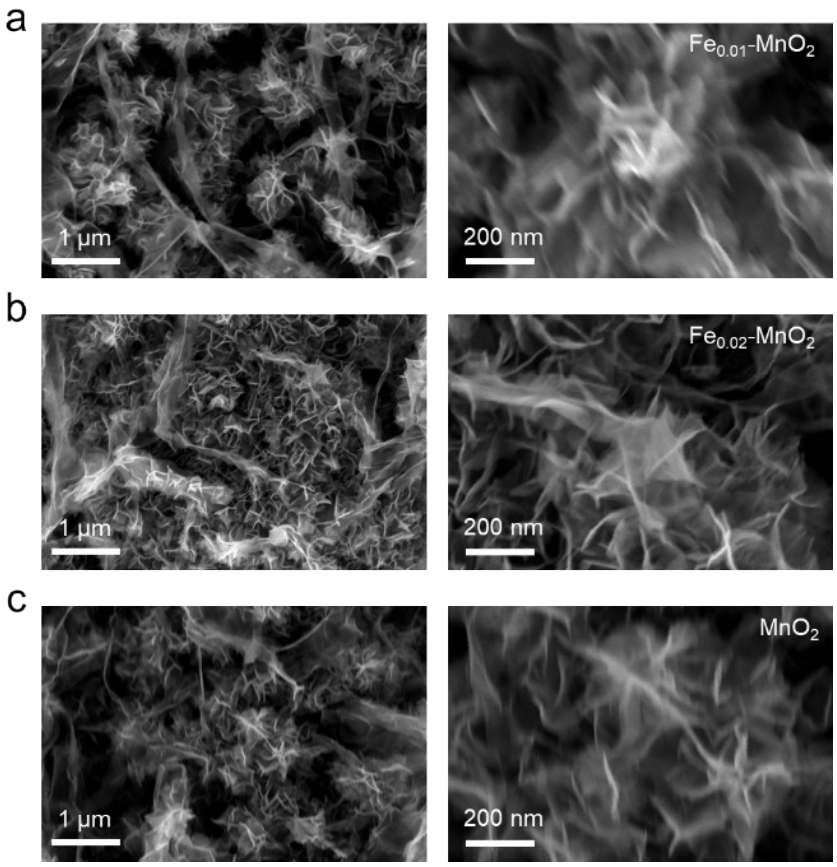

Fig. S8 SEM images of (a) $Fe_{0.01}$-MnO_2, (b) $Fe_{0.02}$-MnO_2, and (c) MnO_2 samples.

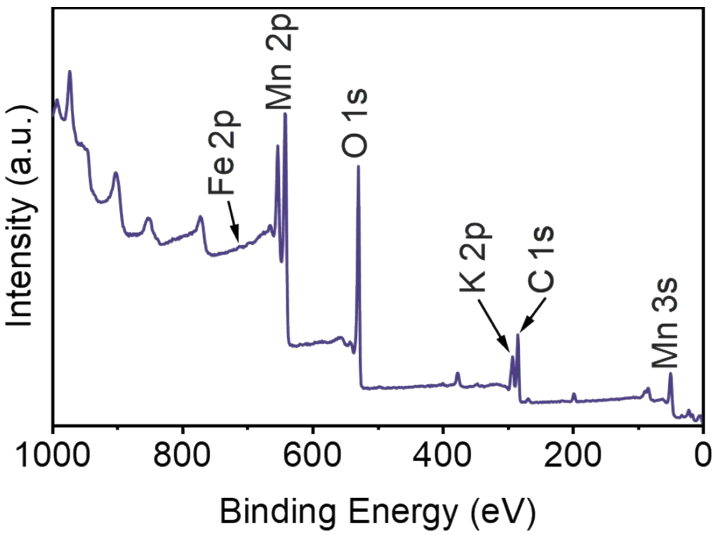

Fig. S9 The total XPS spectrum of Fe-MnO_2.

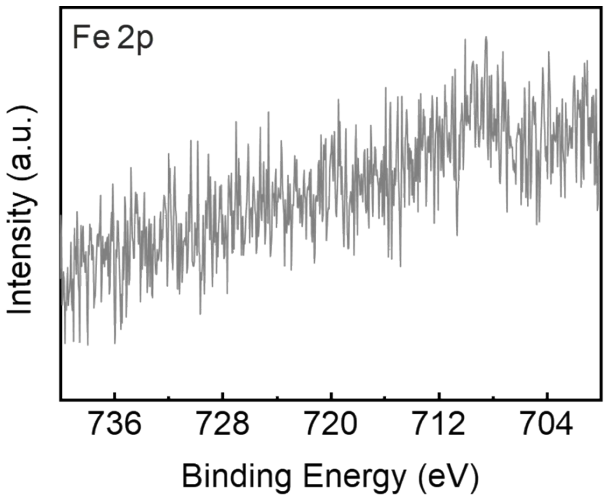

Fig. S10 Fe 2p XPS spectra of Fe-MnO_2 materials.

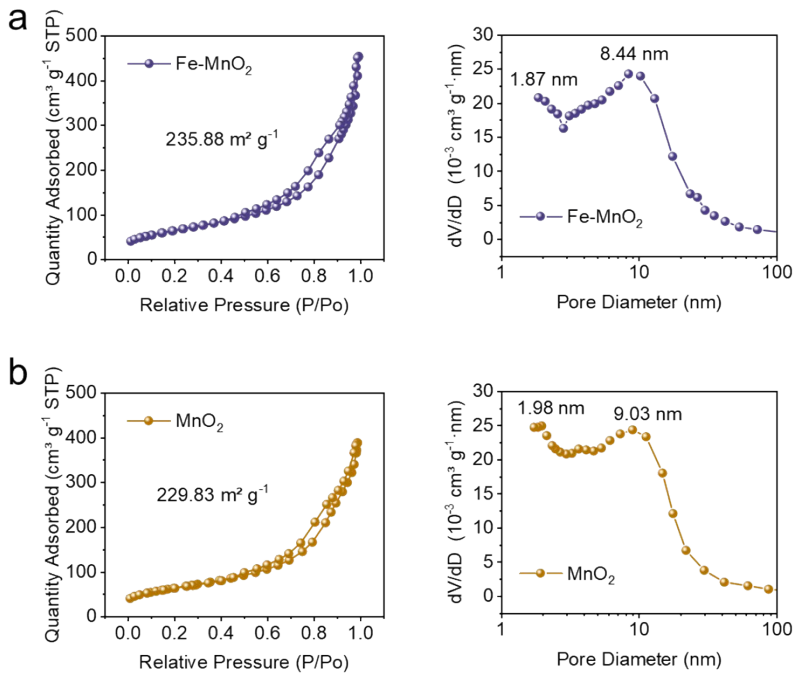

Fig. S11 The nitrogen adsorption-desorption isotherm and pore size distribution of a) Fe-MnO_2 and b) MnO_2 samples.

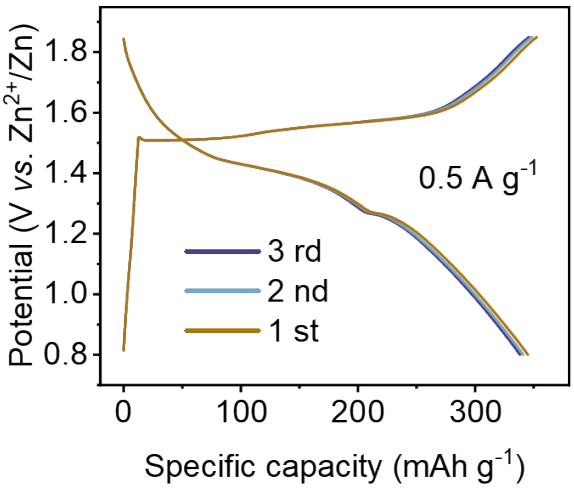

Fig. S12 The GCD curves of Fe-MnO_2 cathode at the current density of 0.5 A g^{-1}.

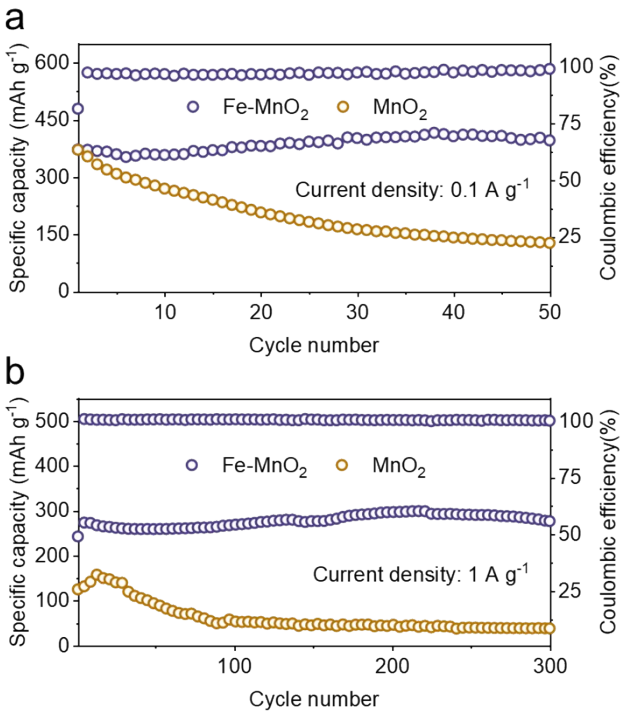

Fig. S13 Cycling performance of Fe-MnO_2 and MnO_2 cathodes at low current of 0.1 and 1 A g^{-1}.

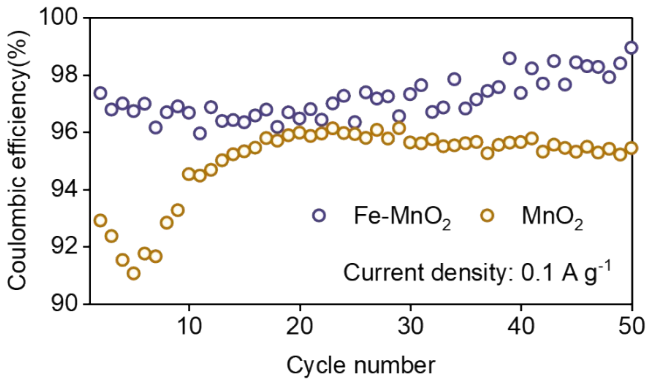

Fig. S14 The CE of Fe-MnO_2 and MnO_2 cathodes at a low rate of 0.1 A g^{-1}.

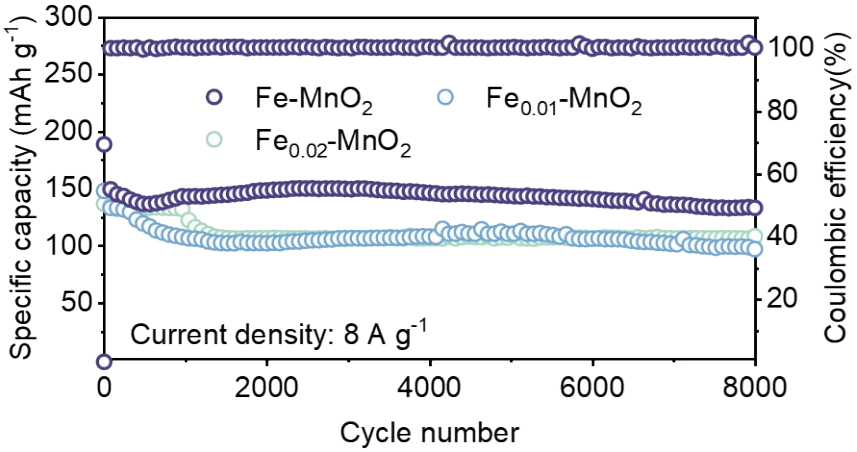

Fig. S15 Cycling abilities at 8 A g^{-1} of Fe-MnO_2, $Fe_{0.01}$-MnO_2 and $Fe_{0.02}$-MnO_2.

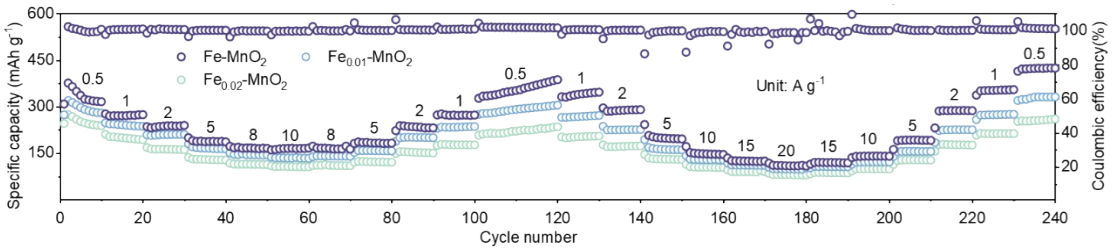

Fig. S16 Rate performance at various current densities of Fe-MnO_2, $Fe_{0.01}$-MnO_2 and $Fe_{0.02}$-MnO_2.

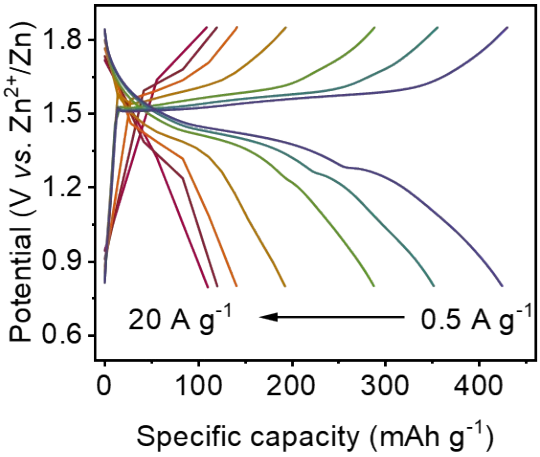

Fig. S17 The GCD curves of Fe-MnO_2 cathode at 0.5-20 A g^{-1}.

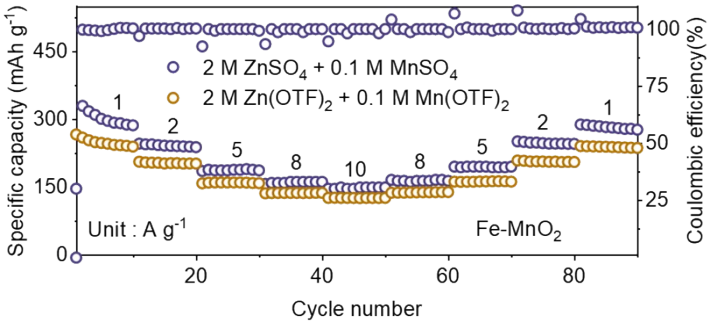

Fig. S18 Rate performance of Fe-MnO_2 cathode in 2 M $Zn(OTF)_2$ + 0.1 M $Mn(OTF)_2$ and 2 M $ZnSO_4$ + 0.1 M $MnSO_4$ electrolytes at various current densities.

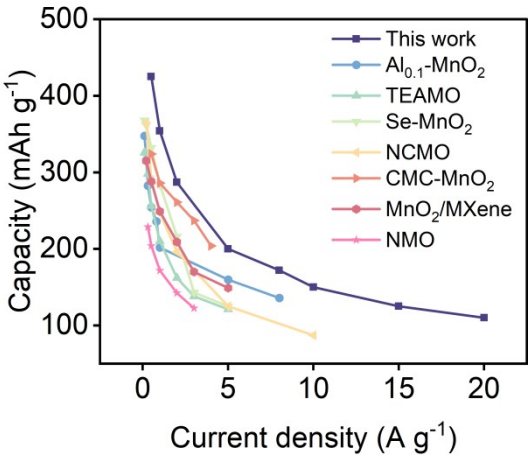

Fig. S19 Comparison of rate performance between Fe-MnO_2 and other cathode materials previously reported in AZIBs (excluding CC mass).

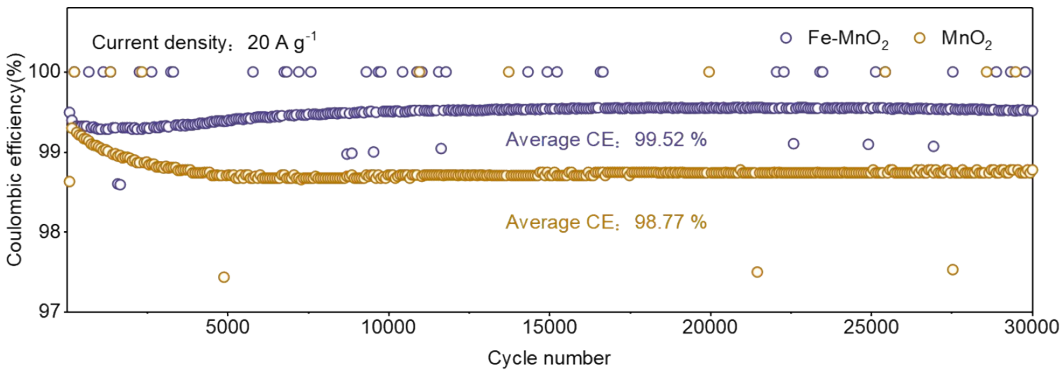

Fig. S20 The CEs of Fe-MnO_2 and MnO_2 cathodes under the 30,000 cycles test.

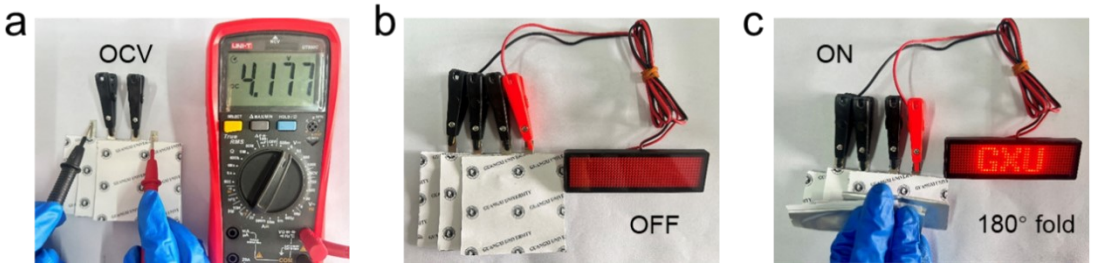

Fig. S21 (a) The OVC of three Zn||Fe-MnO_2 pouch cells. (b) OFF state of LEDs connected to three cells. (c) ON state of LEDs connected to three cells with 180°fold.

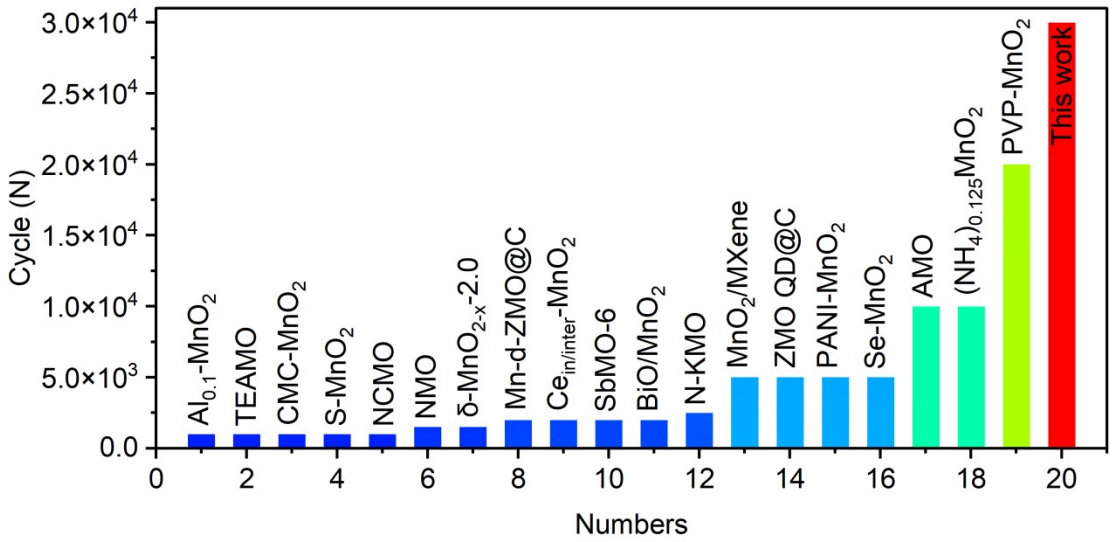

Fig. S22 Comparison of cycling ability between Fe-MnO_2 and other cathode materials previously reported in AZIBs (excluding CC mass).

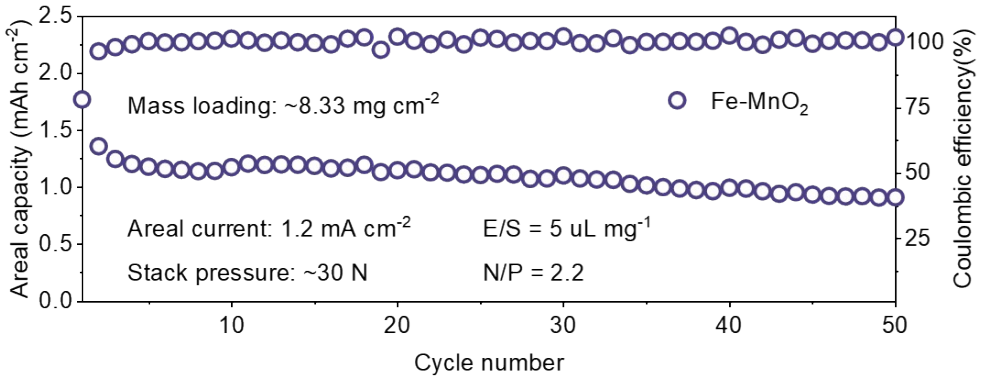

Fig. S23 The performance of Zn||Fe-MnO_2 pouch cell with a high loading of ~8.33 mg cm^{-2} Fe-MnO_2 (porosity: 0.71 cm^3 g^{-1}).

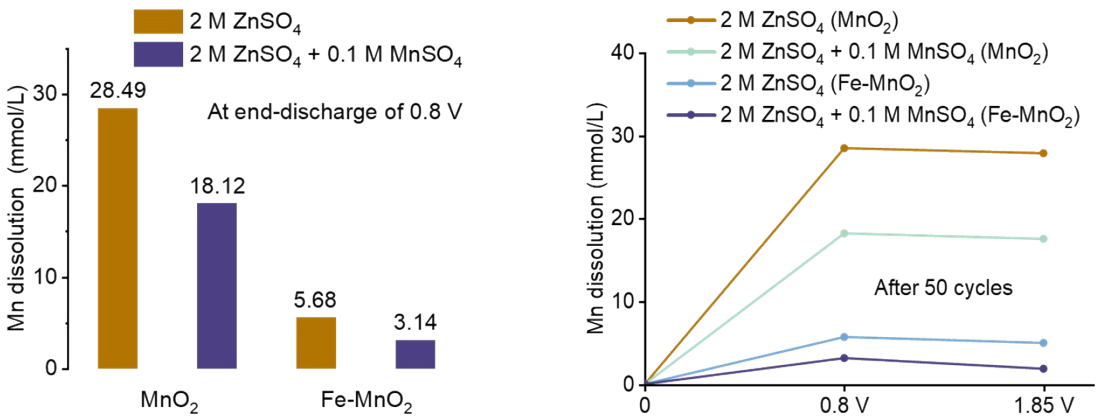

Fig. S24 UV–vis of Fe-MnO_2 and MnO_2 cathodes at the end-discharge and end-charge after 50 cycles in 2 M $ZnSO_4$ and 2 M $ZnSO_4$ + 0.1 M $MnSO_4$ electrolytes.

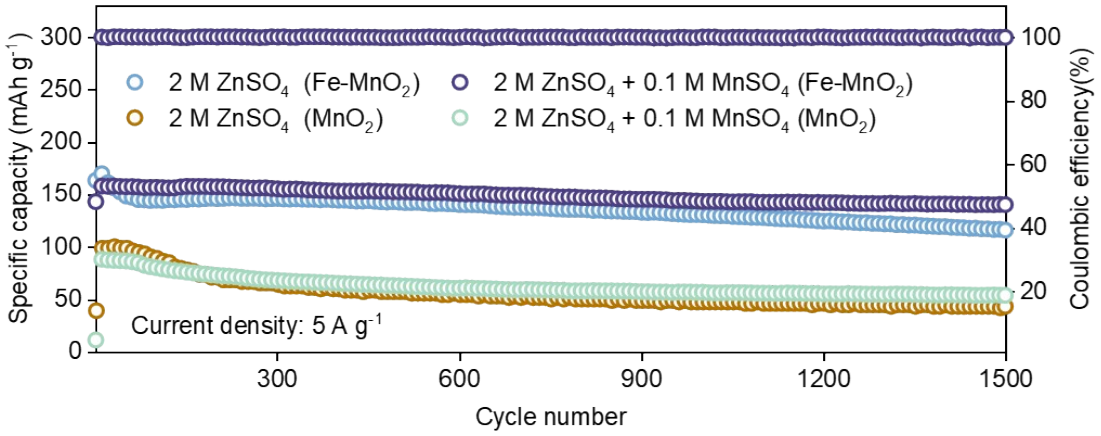

Fig. S25 Cycling test of Fe-MnO_2 and MnO_2 cathodes in 2 M $ZnSO_4$ and 2 M $ZnSO_4$ + 0.1 M $ZnSO_4$ electrolytes.

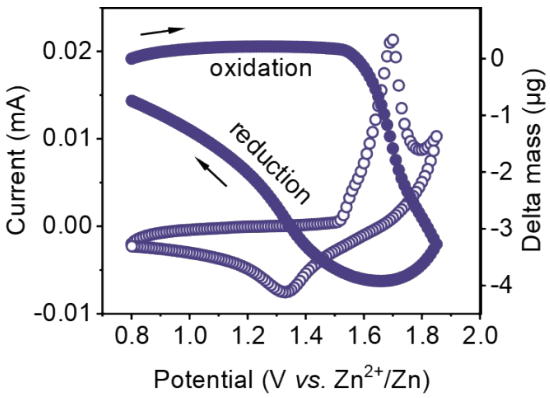

Fig. S26 Results of CV test for the Fe-MnO_2 electrode at 1 mV s^{-1} in 2 M $ZnSO_4$ + 0.1 M $MnSO_4$ electrolytes and the corresponding in situ EQCM measurement results.

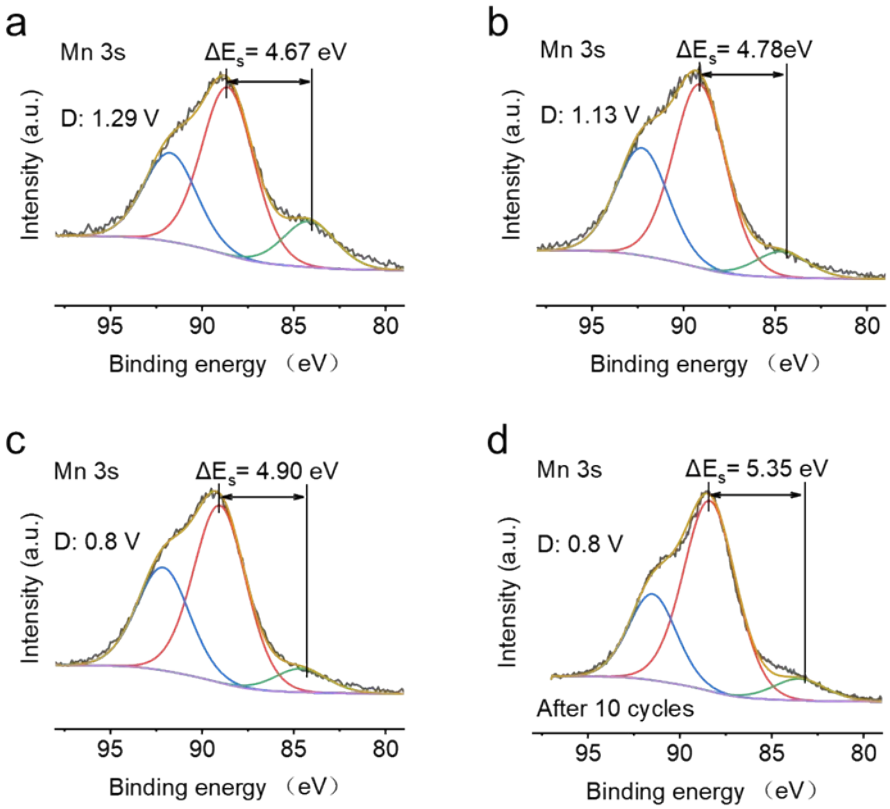

Fig. S27 XPS spectra of Mn 3s at (a-c) 1st and (d) 10th discharge states of Fe-MnO_2 cathode.

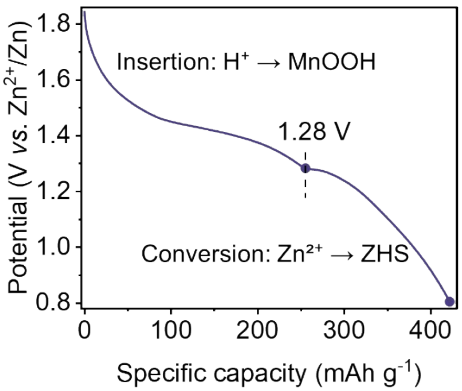

Fig. S28 Capacity contribution partitioning based on insertion and conversion reactions.

Note: The measured capacity of 423 mAh g^{-1} consists of host and non-host processes, where the host process is primarily provided by H^+ insertion and the non-host process consists of Zn^{2+} conversion and Mn^{2+} deposition/dissolution. Integrated with operando XRD analysis, it is inferred that the process primarily involves H^+ insertion before 1.28 V, followed by Zn^{2+} conversion reactions after 1.28 V. Meanwhile, Mn^{2+} deposition and dissolution may accompany the overall redox process. Among which, H^+ insertion is $MnO_2 + H^+ + e^- \rightarrow MnOOH$ and Zn^{2+} conversion is $4Zn^{2+} + 6OH^- + SO_4^{2-} + 5H_2O \rightarrow Zn_4(OH)_6SO_4 \bullet 5H_2O$.

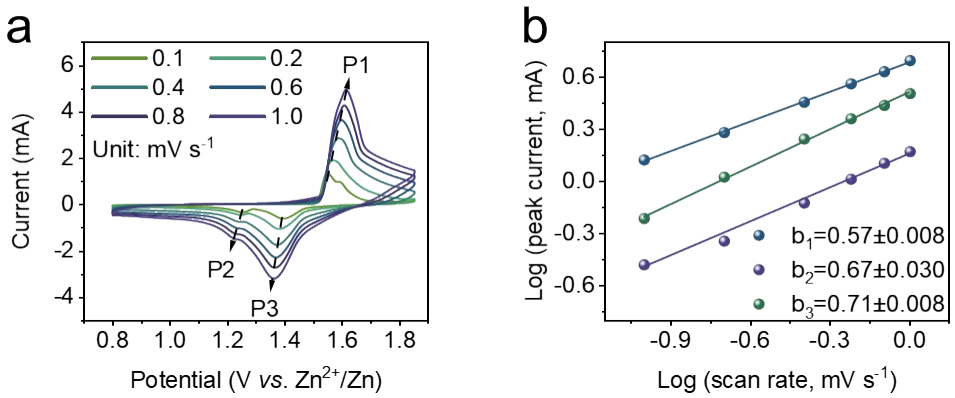

Fig. S29 (a) CV curves at different scan rates and (b) the corresponding log (*i*) versus log (*v*) plots at each redox peak of Fe-MnO_2 cathode.

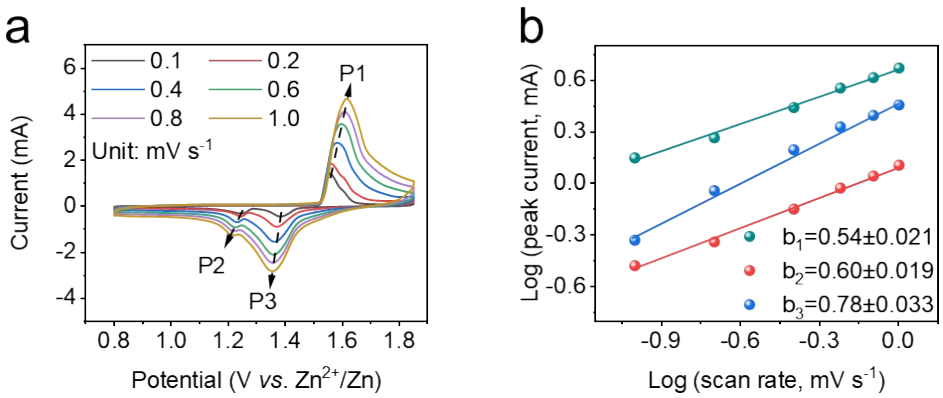

Fig. S30 (a) CV curves at different scan rates and (b) the corresponding log (*i*) versus log (*v*) plots at each redox peak of MnO_2 cathode.

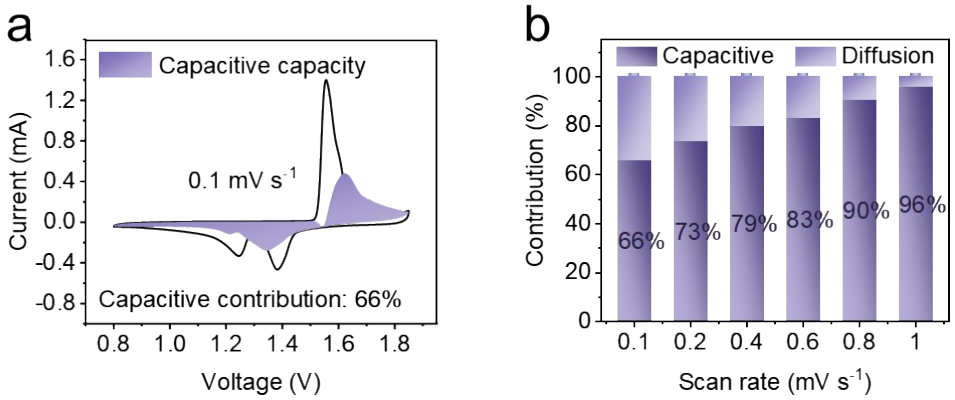

Fig. S31 (a) The capacitive and diffusion-controlled contribution of Fe-MnO_2 cathode at a scan rate of 0.1 mV s^{-1}. (b) Capacitive/diffusive fractions at different scan rates for Fe-MnO_2.

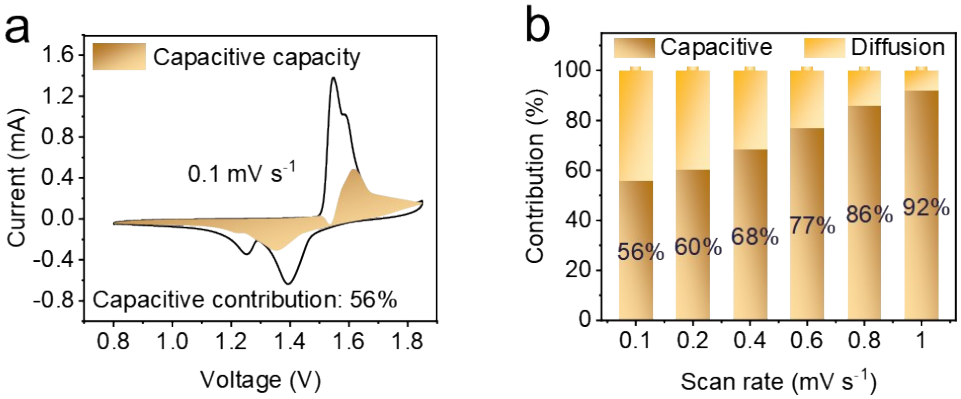

Fig. S32 (a) The capacitive and diffusion-controlled contribution of MnO_2 cathode at a scan rate of 0.1 mV s^{-1}. (b) Capacitive/diffusive fractions at different scan rates for MnO_2.

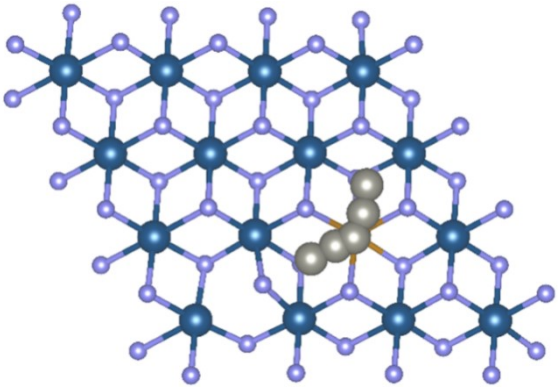

Fig. S33 Zn^{2+} diffusion paths in Fe-MnO_2.

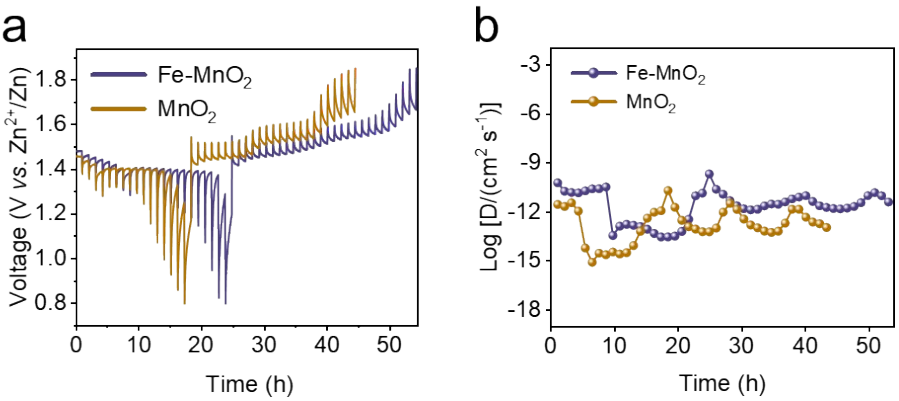

Fig. S34 (a) GITT curves of Fe-MnO_2 and MnO_2 for the charge and discharge process. (b) Corresponding ion diffusion coefficients of Fe-MnO_2 and MnO_2.

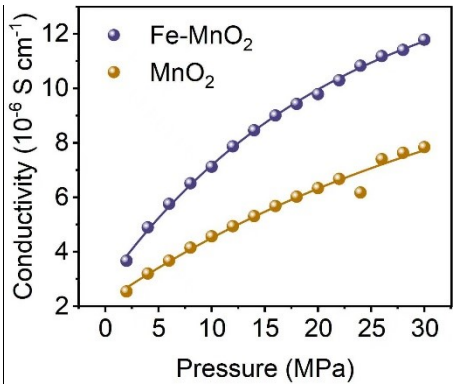

Fig. S35 The conductivity of Fe-MnO_2 and MnO_2 samples by four-probe test.

Note: Electrical conductivity (σ) is obtained as an average value and the R-square of Fe-MnO_2 and MnO_2 are 0.9987 and 0.9816, respectively.

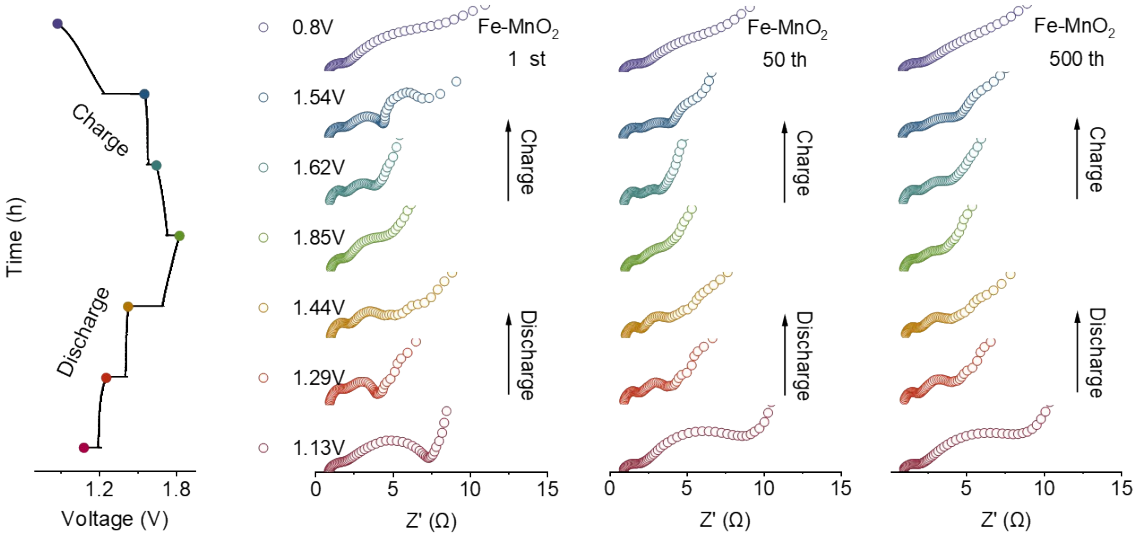

Fig. S36 *In-situ* EIS of Fe-MnO_2 cathode after 1st, 50th, and 500th cycles.

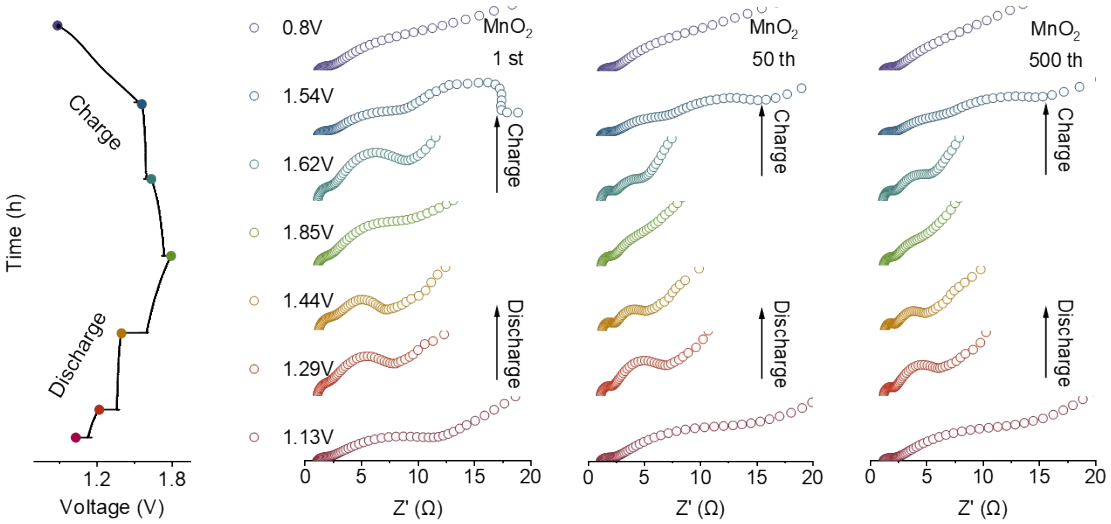

Fig. S37 *In-situ* EIS of MnO_2 cathode after 1st, 50th, and 500th cycles.

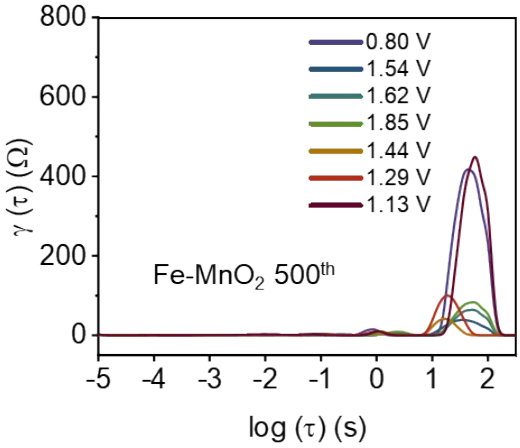

Fig. S38 DRT plots calculated from *In-situ* EIS measurements of Fe-MnO_2 at 500^{th} cycles within the total range of 10^{-5}-$10^{2.5}$ s.

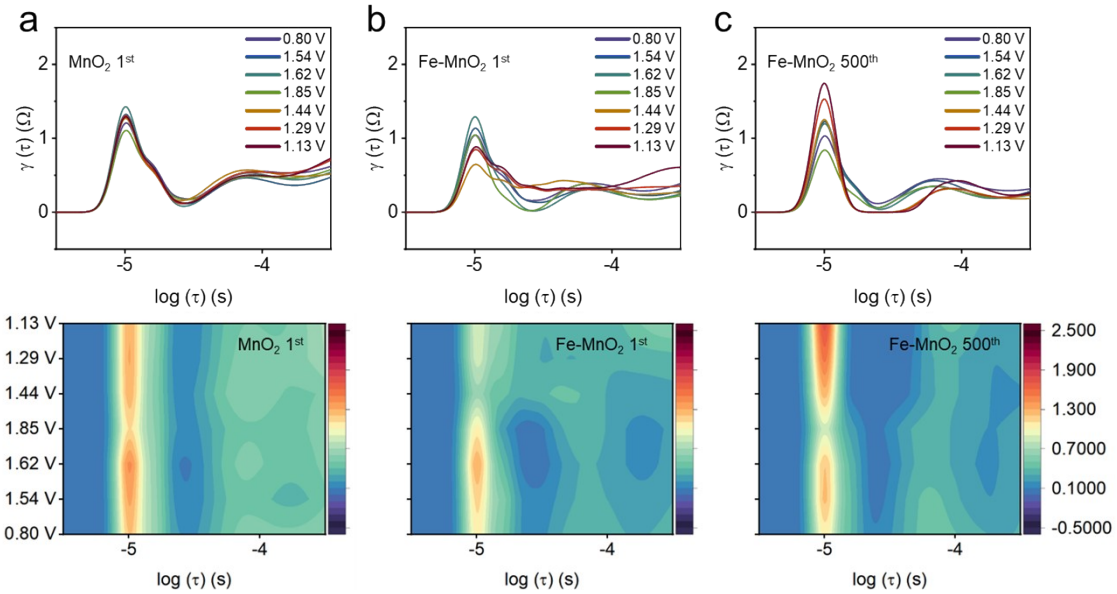

Fig. S39 DRT plots calculated from *In-situ* EIS measurements of (a) MnO_2 at 1st cycle and (b, c) Fe-MnO_2 at 1st and 500th cycles within the range of $10^{-5.5}$-$10^{-3.5}$ s.

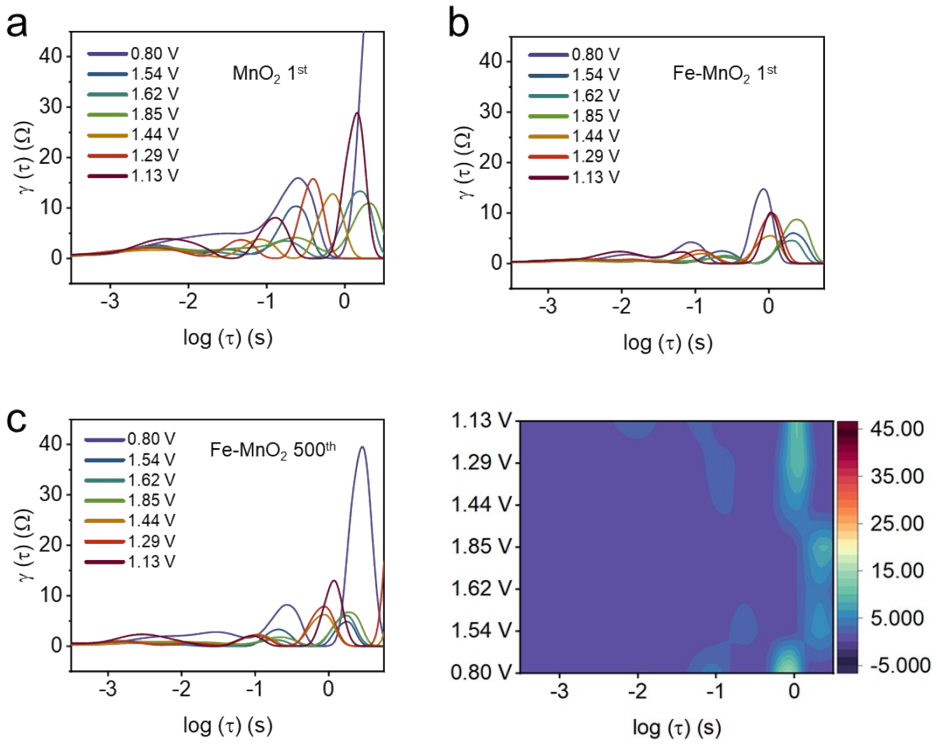

Fig. S40 DRT plots calculated from *In-situ* EIS measurements of (a) MnO_2 at 1st cycle and (b, c) Fe-MnO_2 at 1st and 500th cycles within the range of $10^{-3.5}$-$10^{0.5}$ s.

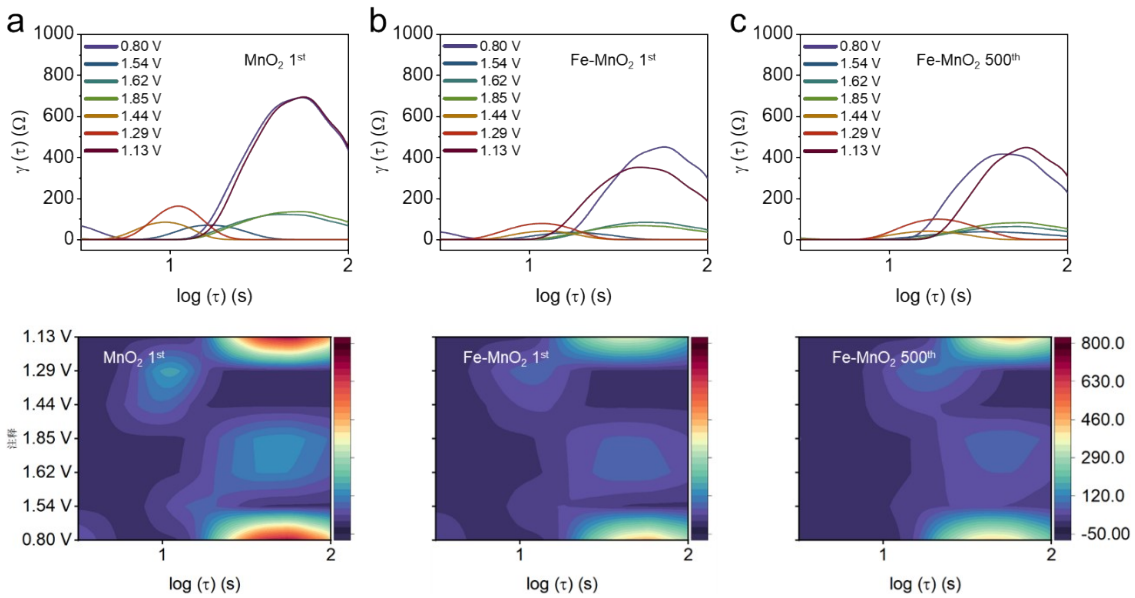

Fig. S41 DRT plots calculated from *In-situ* EIS measurements of (a) MnO_2 at 1st cycle and (b, c) Fe-MnO_2 at 1st and 500th cycles within the range of $10^{0.5}$-10^2 s.

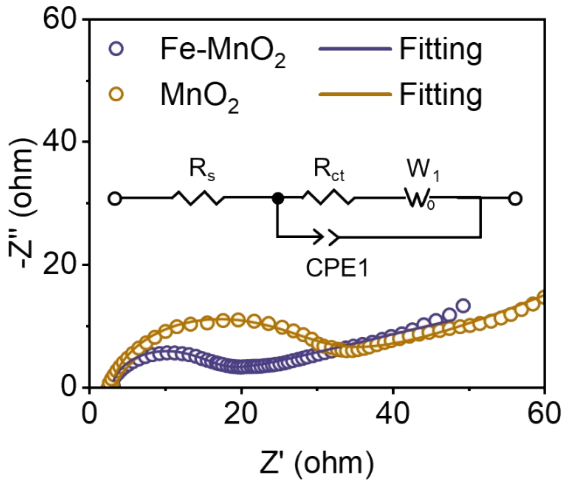

Fig. S42 Nyquist plots of high-load Fe-MnO_2 and MnO_2 cathodes and their equivalent circuit fits.

Table S1. Detailed DFT calculation parameters of M-MnO_2 configurations (M: Fe, Mg, Ca, Ni, Ag, Cu and Co)

Configurations	Functional/U	Spin	Supercell	Bader Workflow
Fe-MnO_2	PBE-GGA/5.3	5	2*2*1	ZAVL-x(Fe)
Mg-MnO_2	PBE-GGA/0	0	2*2*1	ZAVL-x(Mg)
Ca-MnO_2	PBE-GGA/0	0	2*2*1	ZAVL-x(Ca)
Ni-MnO_2	PBE-GGA/6.1	2	2*2*1	ZAVL-x(Ni)
Ag-MnO_2	PBE-GGA/0	0	2*2*1	ZAVL-x(Ag)
Cu-MnO_2	PBE-GGA/7.1	1	2*2*1	ZAVL-x(Cu)
Co-MnO_2	PBE-GGA/3.3	3	2*2*1	ZAVL-x(Co)
MnO_2	PBE-GGA/3.9	3	2*2*1	~

Note:

U: The DFT+U method was used, and U represents the U-value of DFT+U.

Spin: Spin-polarized calculations are performed. The values in the table represent magnetic moments.

The adsorption energies (E_{ads}) were calculated as $E_{ads} = E_{ad/sub} - E_{ad} - E_{sub}$, where $E_{ad/sub}$, E_{ad}, and E_{sub} are the optimized adsorbate/substrate system, the adsorbate, and the clean substrate, respectively.

The dissolution energies (E_{dis}) were calculated as $E_{dis} = E_{sub} - (E_{sub/Mn(n-1)} + \mu_{Mn})$, where E_{sub}, $E_{sub/Mn(n-1)}$, and μ_{Mn} are the optimized substrate system, the substrate lacking a Mn atom, and the chemical potential of Mn, respectively.

Bader Workflow: Bader charge transfer values = ZAVL-x(M), where ZAVL and x(M) are the number of valence electrons in metal atom and the Net charge on a metal atom.

Table S2. The results of ICP-OES testing for three batches of Fe-MnO_2

Samples	NO. 1	NO. 2	NO. 3
Fe/(Fe+Mn)	12.86 %	13.14 %	13.15 %

Note:

The conversion between mass fraction and molar percentage follows the process:

$W_{Fe}/M_{Fe}=N_{Fe}$ $W_{Mn}/M_{Mn}=N_{Mn}$

$Fe/(Fe+Mn) = N_{Fe}/(N_{Fe} + N_{Mn})*100\%$

Where W is the mass fraction (wt.%), M is the relative atomic mass, and N is the relative molar number (mol), and Fe/(Fe+Mn) signifies the molar percentage.

Table S3. The EXAFS fitting results of Fe-MnO_2

Sample	Bond	R(Å)	CN	$\sigma^2(10^{-3}$ Å$^2)$	ΔE_0(eV)	R factor
Fe	Fe-O	1.94±0.02	5.4±1.2	4.2±2.7	-2.8±2.6	0.0197

Table S4. The comparison for Fe-MnO_2 and other cathodes in AZIBs

Material/windows	Mass loading/electrolyte	Rate	Cycling	Ref.
$Al_{0.1}$-MnO_2/ 0.8–1.8 V	~1.5 mg/ 2.0 M $ZnSO_4$ + 0.1 M $MnSO_4$	348 mAh g^{-1} at 0.1 A g^{-1} 136 mAh g^{-1} at 8 A g^{-1}	202 mAh g^{-1} at 1 A g^{-1} (1000 cycles)	4
AMO/ 0.8–1.8 V	1-1.5 mg cm^{-2}/ 2.0 M $ZnSO_4$ + 0.1 M $MnSO_4$	419 mAh g^{-1} at 0.5 A g^{-1} 56 mAh g^{-1} at 8 A g^{-1}	129 mAh g^{-1} at 4 A g^{-1} (10000 cycles)	5
PVP-MnO_2/ 0.8–1.8 V	0.75-1.5 mg cm^{-2}/ 2 M $ZnSO_4$ + 0.2 M $MnSO_4$	317 mAh g^{-1} at 0.125 A g^{-1} 106 mAh g^{-1} at 12.5 A g^{-1}	140 mAh g^{-1} at 10 A g^{-1} (20000 cycles)	6
TEAMO/ 1.0–1.8 V	0.5-1.5 mg cm^{-2}/ 2.0 M $ZnSO_4$ + 0.1 M $MnSO_4$	351 mAh g^{-1} at 0.1 A g^{-1} 121 mAh g^{-1} at 5 A g^{-1}	105 mAh g^{-1} at 1 A g^{-1} (1000 cycles)	7
Se-MnO_2/ 0.8–1.8 V	1.2 mg cm^{-2}/ 2.0 M $ZnSO_4$ + 0.1 M $MnSO_4$	368 mAh g^{-1} at 0.1 A g^{-1} 125 mAh g^{-1} at 5 A g^{-1}	102 mAh g^{-1} at 3 A g^{-1} (5000 cycles)	8
CMC-MnO_2/ 0.8–1.8 V	1.2 mg (1.13 cm^{-2})/ 2 M $ZnSO_4$ + 0.2 M $MnSO_4$	324 mAh g^{-1} at 0.5 A g^{-1} 204 mAh g^{-1} at 4 A g^{-1}	215 mAh g^{-1} at 1.5 A g^{-1} (1000 cycles)	9
S-MnO_2/ 0.8–1.8 V	1-1.4 mg cm^{-2}/ 2.0 M $ZnSO_4$ + 0.1 M $MnSO_4$	324 mAh g^{-1} at 0.2 A g^{-1} 205 mAh g^{-1} at 2 A g^{-1}	150 mAh g^{-1} at 3 A g^{-1} (1000 cycles)	10
PANI-MnO_2/ 1.0–1.8 V	2.0 mg cm^{-2}/ 2.0 M $ZnSO_4$ + 0.1 M $MnSO_4$	280 mAh g^{-1} at 0.2 A g^{-1} 110 mAh g^{-1} at 3 A g^{-1}	125 mAh g^{-1} at 2 A g^{-1} (5000 cycles)	11
N-KMO/ 1.0–1.8 V	1 mg cm^{-2}/ 2.0 M $ZnSO_4$ + 0.1 M $MnSO_4$	298 mAh g^{-1} at 0.1 A g^{-1} 106 mAh g^{-1} at 10 A g^{-1}	262 mAh g^{-1} at 1 A g^{-1} (2500 cycles)	12
ZMO QD@C/ 1.0–1.8 V	None/None	298 mAh g^{-1} at 0.175 A g^{-1} 124.5 mAh g^{-1} at 3.5 A g^{-1}	100.9 mAh g^{-1} at 3.5 A g^{-1} (5000 cycles)	13
NHMO/ 0.4–1.9 V	1-2 mg cm^{-2}/ 2.0 M $ZnSO_4$ + 0.1 M $MnSO_4$	329 mAh g^{-1} at 0.15 A g^{-1} 109 mAh g^{-1} at 6 A g^{-1}	109 mAh g^{-1} at 6.0 A g^{-1} (10000 cycles)	14
NMO/ 1.0–1.8 V	~1.0 mg cm^{-2}/ 2.0 M $ZnSO_4$ + 0.1 M $MnSO_4$	228.7 mAh g^{-1} at 0.3 A g^{-1} 122.5 mAh g^{-1} at 3 A g^{-1}	141.4 mAh g^{-1} at 2 A g^{-1} (1500 cycles)	15
Mn-d-ZMO@C/ 0.8–1.9 V	None/ 2 M $ZnSO_4$ + 0.2 M $MnSO_4$	233 mAh g^{-1} at 0.1 A g^{-1} 132 mAh g^{-1} at 3 A g^{-1}	82.7 mAh g^{-1} at 3 A g^{-1} (2000 cycles)	16
NCMO/ 0.8–1.9 V	~1 mg cm^{-2}/ 2 M $ZnSO_4$ + 0.2 M $MnSO_4$	364 mAh g^{-1} at 0.2 A g^{-1} 84 mAh g^{-1} at 10 A g^{-1}	200 mAh g^{-1} at 2 A g^{-1} (1000 cycles)	17
$Ce_{in/inter}$-MnO_2/ 0.9–1.8 V	1~2 mg cm^{-2}/ 2 M $ZnSO_4$ + 0.1 M $MnSO_4$	270.9 mAh g^{-1} at 0.3 A g^{-1} 140.5 mAh g^{-1} at 3 A g^{-1}	148.9 mAh g^{-1} at 3 A g^{-1} (2000 cycles)	18

δ-MnO_{2-x}-2.0/ 0.9–1.9 V	None	551.8 mAh g^{-1} at 0.5 A g^{-1} 262.2 mAh g^{-1} at 10 A g^{-1}	~332 mAh g^{-1} at 3 A g^{-1} (1500 cycles)	19
MnO_2/MXene/ 0.8–1.8 V	~1.5 mg cm^{-2}/ 2.0 M $ZnSO_4$ + 0.1 M $MnSO_4$	315 mAh g^{-1} at 0.2 A g^{-1} 149 mAh g^{-1} at 5 A g^{-1}	132 mAh g^{-1} at 5 A g^{-1} (5000 cycles)	20
SbMO-6/ 0.8–1.8 V	~1 mg cm^{-2}/ 2.0 M $ZnSO_4$ + 0.2 M $MnSO_4$	221.8 mAh g^{-1} at 0.1 A g^{-1} 125 mAh g^{-1} at 5 A g^{-1}	113 mAh g^{-1} at 2 A g^{-1} (2000 cycles)	21
BiO/MnO_2/ 0.8–1.9 V	1 ~ 2 mg cm^{-2}/ 3.0 M $ZnSO_4$ + 0.5 M $MnSO_4$	720.6 mAh g^{-1} at 0.1 A g^{-1} 204.5 mAh g^{-1} at 4 A g^{-1}	161 mAh g^{-1} at 2 A g^{-1} (2000 cycles)	22
Fe-MnO_2/ 0.8–1.85 V	**0.8-1.2 mg/ 2.0 M $ZnSO_4$ + 0.1 M $MnSO_4$**	**423 mAh g^{-1} at 0.5 A g^{-1} 109 mAh g^{-1} at 20 A g^{-1}**	**112 mAh g^{-1} at 20 A g^{-1} (30000 cycles)**	**This work**

Note: All performance data are calculated based on the mass of the active materials (excluding carbon cloth or other substrates).

Table S5. The comparison for Fe-MnO_2 and other cathodes in AZIBs of cycling, rate, CE, capacity (at 0.5 A g^{-1}), and retention

Material/ windows	Mass loading/ electrolyte	Cycle (k)	Retention (%)	Capacity (mAh g^{-1})	CE (%)	Rate (A g^{-1})	Ref.
Al-MnO_2/ 0.8–1.8 V	~1.5 mg/ 2.0 M $ZnSO_4$ + 0.1 M $MnSO_4$	1	87	254.3	~100	8	4
AMO/ 0.8–1.8 V	1-1.5 mg cm^{-2}/ 2.0 M $ZnSO_4$ + 0.1 M $MnSO_4$	10	69	419	~100	8	5
NiMn-LDHv/ 0.8–1.9 V	None/ 2.0 M $ZnSO_4$ + 0.1 M $MnSO_4$	2.5	91	224	~100	11	23
Se-MnO_2/ 0.8–1.8 V	1.2 mg cm^{-2}/ 2.0 M $ZnSO_4$ + 0.1 M $MnSO_4$	5	~100	332	~100	5	8
PVP-MnO_2/ 0.8–1.8 V	0.75-1.5 mg cm^{-2}/ 2 M $ZnSO_4$ + 0.2 M $MnSO_4$	20	~100	250	~100	12.5	6
Ce-MnO_2/ 0.9–1.8 V	1~2 mg cm^{-2}/ 2 M $ZnSO_4$ + 0.1 M $MnSO_4$	2	~100	279.7	~100	3	18
CMC-MnO_2/ 0.8–1.8 V	1.2 mg (1.13 cm^{-2})/ 2 M $ZnSO_4$ + 0.2 M $MnSO_4$	1	86.2	324	~100	4	9
IS-MnO_2/ 0.8–1.8 V	None/ 2.0 M $ZnSO_4$ + 0.1 M $MnSO_4$	4	90.3	230	~100	6	24
Fe-MnO_2/ 0.8–1.85 V	**0.8-1.2 mg/ 2.0 M $ZnSO_4$ + 0.1 M $MnSO_4$**	**30**	**89**	**423**	**~100**	**20**	**This work**

Note: All performance data are calculated based on the mass of the active materials (excluding carbon cloth or other substrates).

Table S6. Relevant parameters of the Mott-Schottky measurement

Sample	Frequency	AC amplitude	Dielectric constant	Area determination	R square
Fe-MnO_2	1.5 kHz	10 mV	5	1 cm^2	0.998
MnO_2	1.5 kHz	10 mV	5	1 cm^2	0.990

Note: The dielectric constant is relative to the vacuum dielectric constant (8.854×10^{-12} F m^{-1}). The area determination is the geometric area of the conductive glass on which the coating is applied.

Table S7. Relevant parameters of the four-probe measurement

σ(Fe-MnO_2) S cm^{-1}	σ(MnO_2) S cm^{-1}	Pressure Mpa	Temperature ℃	Humidity % RH
3.67E-06	2.54E-06	2	25	65
4.89E-06	3.20E-06	4	25	65
5.76E-06	3.67E-06	6	25	65
6.51E-06	4.15E-06	8	25	65
7.12E-06	4.57E-06	10	25	65
7.87E-06	4.94E-06	12	25	65
8.46E-06	5.31E-06	14	25	65
9.00E-06	5.68E-06	16	25	65
9.43E-06	6.02E-06	18	25	65
9.79E-06	6.34E-06	20	25	65
1.03E-05	6.66E-06	22	25	65
1.08E-05	6.17E-06	24	25	65
1.12E-05	7.40E-06	26	25	65
1.14E-05	7.64E-06	28	25	65
1.18E-05	7.84E-06	30	25	65

Table S8. Results of equivalent circuit fit for Fe-MnO_2 cathode and related parameters

Fe-MnO_2	R_s (Ω)	R_{ct} (Ω)	CPE1	CIs
Value	3.04	8.09	0.93	0.45 %
Residuals	2.52 %	12.30 %	2.16 %	~

Table S9. Results of equivalent circuit fit for MnO_2 cathode and related parameters

MnO_2	R_s (Ω)	R_{ct} (Ω)	CPE1	CIs
Value	2.97	14.6	0.90	0.21 %
Residuals	2.46 %	7.21 %	1.20 %	~

Reference

1. W. Kohn and L. J. Sham, *Phys. Rev.*, 1965, **140**, A1133-A1138.
2. G. Kresse and J. Hafner, *Phy. Rev. B*, 1993, **47**, 558-561.
3. G. Henkelman, B. P. Uberuaga and H. Jónsson, *J. Chem. Phys.*, 2000, **113**, 9901-9904.
4. Y. Zhao, S. Zhang, Y. Zhang, J. Liang, L. Ren, H. J. Fan, W. Liu and X. Sun, *Energy Environ. Sci.*, 2024, **17**, 1279-1290.
5. H. Yao, H. Yu, Y. Zheng, N. W. Li, S. Li, D. Luan, X. W. D. Lou and L. Yu, *Angew. Chem. Int. Ed.*, 2023, **62**, e202315257.
6. A. Zhang, R. Zhao, Y. Wang, J. Yue, J. Yang, X. Wang, C. Wu and Y. Bai, *Angew. Chem. Int. Ed.*, 2023, **62**, e202313163.
7. S. Wang, S. Yao, N. Dai, W. Fu, Y. Liu, K. Ji, Y. Ji, J. Yang, R. Liu, X. Li, J. Xie, Z. Yang and Y.-M. Yan, *Angew. Chem. Int. Ed.*, 2024, **63**, e202408414.
8. J. J. Ye, P. H. Li, Z. Hou, W. Zhang, W. Zhu, S. Jin and H. Ji, *Angew. Chem. Int. Ed.*, 2024, **63**, e202410900.
9. X. Zhang, X. Ma, H. Bi, Y. Zhang, P. Mi, F. Liu, X. Jin, Y. Chen, K. Zhang, J. Wang and Y. Dong, *Adv. Funct. Mater.*, 2024, **35**, 2411990.
10. Y. Zhao, P. Zhang, J. Liang, X. Xia, L. Ren, L. Song, W. Liu and X. Sun, *Energy Storage Mater.*, 2022, **47**, 424-433.
11. J. Huang, Z. Wang, M. Hou, X. Dong, Y. Liu, Y. Wang and Y. Xia, *Nat. Commun.*, 2018, **9**, 2906.
12. G. Cui, Y. Zeng, J. Wu, Y. Guo, X. Gu and X. W. Lou, *Adv. Sci.*, 2022, **9**, 2106067.
13. S. Deng, Z. Tie, F. Yue, H. Cao, M. Yao and Z. Niu, *Angew. Chem. Int. Ed.*, 2022, **61**, e202115877.
14. T. Sun, S. Zheng, Q. Nian and Z. Tao, *Small*, 2022, **18**, 2107115.
15. S. Wang, X. Zhao, H. Chen, J. Guo, R. Liu and D. a. Yang, *EcoMat*, 2022, **4**, e12249.
16. S. Islam, M. H. Alfaruqi, D. Y. Putro, S. Park, S. Kim, S. Lee, M. S. Ahmed, V. Mathew, Y.-K. Sun, J.-Y. Hwang and J. Kim, *Adv. Sci.*, 2021, **8**, 2002636.
17. X. Gao, C. Shen, H. Dong, Y. Dai, P. Jiang, I. P. Parkin, H. Zhang, C. J. Carmalt and G. He, *Energy Environ. Sci.*, 2024, **17**, 2287-2297.
18. Y. Chen, C. Lin, X. Chen, Z. Lu, K. Zhang, Y. Liu, J. Wang, G. Han and G. Xu, *Adv. Energy Mater.*, 2024, **14**, 2304303.
19. Y. Wang, Y. Zhang, G. Gao, Y. Fan, R. Wang, J. Feng, L. Yang, A. Meng, J. Zhao and Z. Li, *Nano-micro Lett.*, 2023, **15**, 219.
20. Y. Wang, L. Liu, Y. Wang, J. Qu, Y. Chen and J. Song, *ACS Nano*, 2023, **17**, 21761-21770.
21. H. Huang, H. Feng, Z. He, Y. Huang, J. Xu, C. Hu, Z. Chen, Z. Yang and W. Zhang, *ACS Nano*, 2024, **18**, 25601-25613.
22. X. Zhao, F. Zhang, H. Li, H. Dong, C. Yan, C. Meng, Y. Sang, H. Liu, Y.-G. Guo and Shuhua Wang, *Energy Environ. Sci.*, 2024, **17**, 3629-3640.
23. J. Li, X. Yang, J. Wang, C. Ma, T. Wang, N. Liu, X. Pang, Q. Zhang, C. Wu and X. Li, *Energy Storage Mater.*, 2025, **74**, 103887.
24. X. Li, D. He, Q. Zhou, X. Zhou, Z. Wang, C. Wei, Y. Shi, X. Hu, B. Huang, Z. Yang, X. Han, Y. Lin and Y. Yu, *Energy Environ. Sci.*, 2024, **17**, 9195.